ADVANCED FUNCTIONAL MATERIALS
www.afm-journal.de

Tailoring Aerogels and Related 3D Macroporous Monoliths for Interfacial Solar Vapor Generation

*Xiaozhen Hu and Jia Zhu**

Interfacial solar vapor generation is emerging as a promising water treatment technology with high solar energy efficiency and minimized carbon footprint. Among various kinds of materials development, aerogels, with inherent high porosity, lightweight, enhanced absorption, and minimized thermal conductivity, are attracting significant attention for achieving high-performance solar vapor generation. Herein, recent progress in tailoring aerogels (such as graphene [oxide], carbon nanotubes, and polymer aerogels) and related 3D macroporous architectures for interfacial solar vapor generation is presented. Furthermore, the challenges and opportunities associated with employing aerogels in solar vapor generation are also discussed.

1. Introduction

Aerogels are one novel kind of porous solids, which are made more of air than of gel, as the name implies. Since Kistler first synthesized aerogel in 1931,[1] many kinds of aerogels were fabricated, such as SiO_2 aerogels,[2,3] polymer aerogels,[4] metal/metal oxide aerogels,[5] carbon nanotubes (CNTs) aerogels,[6] graphene aerogels,[7,8] and so on. Aerogels possess various unique features including high porosity (>85%),[9–11] lightweight (<0.5 g cm^{-3}),[9–11] large surface area (>50 m^2 g^{-1}), and thermal-insulating property,[12] widely applied in a range of fields like catalysis,[13] sensors,[14] energy storage,[15] and adsorption.[16]

Recently, interfacial solar vapor generation is intensely pursued as one of the most promising technologies to provide portable clean water solution for water-stressed area.[17–21] With carefully tailored solar absorbers, the energy of solar irradiation can be absorbed and converted into heat, which can be utilized to vaporize water in the interfacial area of water and air. As heat energy is localized in the interfacial region, rather than heating the whole bulk water, the efficiency of solar to vapor can be significantly enhanced in interfacial solar vapor generation compared with conventional solar evaporation technology. Combined with the condensation system, clean drinking water can be successfully obtained.[18] To quantitatively evaluate the performance of absorbers, solar thermal conversion efficiency is defined as:

$$\eta = mh_{fg}/q_{solar}A \tag{1}$$

where m is the mass flux of vapor (water evaporation rate, usually calculated from the mass change curve of water), h_{fg} denotes the liquid–vapor phase change enthalpy, q_{solar} is the solar flux per area, and A is the surface area of the absorber facing the sun.[17,18,22] The evaporation rate m can also be expressed as the following equation from the energy point of view:

$$mh_{fg} = A\alpha q_{solar} - Aq_{water} - Ah(T - T_\infty) - A\varepsilon\sigma\left(T^4 - T_\infty^4\right) \tag{2}$$

where α is the solar absorbance, q_{water} is the heat flux to the underlying water, including conduction and radiation, h is the convection heat transfer coefficient, ε is the emittance of the absorbing surface, σ is the Stefan–Boltzmann constant, T is the temperature of absorber, and T_∞ is the temperature of environment.[22]

According to energy analysis of the system (**Figure 1**, Equation (2)), there are several requirements essential for efficient solar vapor generation. First, broadband and efficient solar absorption ($\alpha\uparrow$), which can directly improve the solar energy input, is premise to achieve high energy conversion efficiency. Second, selective absorbers ($\varepsilon\downarrow$) with low thermal conductivity ($\lambda\downarrow$, $q_{water} \sim \lambda\frac{dT}{dx}$) are more favorable to reduce heat losses through thermal conduction, convection, or irradiation. Additionally, good wettability as well as porous structure is necessary to provide expressway for transporting water and channels for rapid vapor escape.

As tailored highly porous structures, aerogels possess several intrinsic advantages ideal for interfacial solar vapor generation. First, the porous and nanoscale rough morphology of aerogels can not only reduce the light reflection but also enhance light

Dr. X. Z. Hu
Jiangsu Key Laboratory of Atmospheric Environment Monitoring and Pollution Control
Jiangsu Collaborative Innovation Center of Atmospheric Environment and Equipment Technology
Jiangsu Engineering and Technology Research Center of Environmental Cleaning Materials, and School of Environmental Science and Engineering
Nanjing University of Information Science and Technology
219 Ningliu Road, Nanjing 210044, China
Prof. J. Zhu
National Laboratory of Solid State Microstructures
College of Engineering and Applied Sciences, and Collaborative Innovation Center of Advanced Microstructures
Nanjing University
16 Jinyin Street, Nanjing 210093, China
E-mail: jiazhu@nju.edu.cn
The ORCID identification number(s) for the author(s) of this article can be found under https://doi.org/10.1002/adfm.201907234.

DOI: 10.1002/adfm.201907234

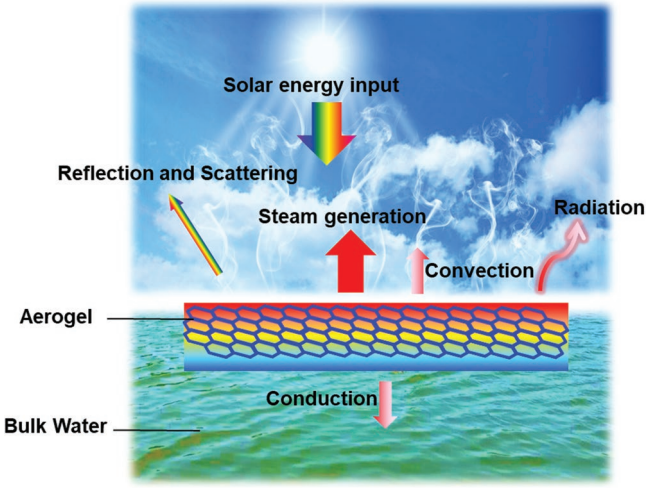

Figure 1. Schematic illustration of tailoring aerogels for interfacial solar vapor generation.

scattering inside pores of aerogels, improving the absorption of solar energy. Second, highly porous characteristics (porosity >85%) induces low thermal conductivity,[4,23,24] which can effectively confine the generated heat in the interfacial region of water and air, and reduce conduction heat loss of the system. Third, owing to the porous structure, the air and vapor inside aerogels was separated into small units, highly reducing the macroscopic heat convection. Lastly, the interconnected pores inside aerogels can offer plenty of channels for fast water transportation and vapor escape, which also endow aerogels lightweight property (<0.5 g cm^{-3}), making aerogels naturally float on water surface without any support.

In the past few years, aerogels and related 3D macroporous monoliths have been widely investigated for interfacial solar vapor generation, achieving enhanced energy conversion efficiency.[25–50] In this progress report, we will summarize the developments of aerogels and related 3D macroporous architectures for interfacial solar vapor generation, mainly from four aspects, including tailoring nanostructure of pores by tuning building block and synthesis parameters; optical management of different aerogel absorbers including carbon nanomaterials, carbonized materials, plasmonic nanoparticles, and other absorbers; thermal management through materials design and device design; and wettability enhancement. Specific examples are provided to illustrate these fundamental design principles. In addition, a future prospect of aerogels for interfacial solar vapor generation is also discussed.

2. Tailoring Pore Structure

Aerogels are one kind of the most promising evaporators for efficient solar vapor generation attributing to the highly porous structure (porosity >85%), which is the fundamental element for all the advantages including lightweight (<0.5 g cm^{-3}), enhanced absorption, decreased thermal conductivity, and so on. Due to the high porosity and extremely low density, aerogels can not only naturally self-float on water surface, but also provide channels for water transportation and vapor escape. In this section, we will focus on tailoring pore structure of aerogel absorbers including pore shape, size, and porosity to improve the solar evaporation efficiency mainly from the following two aspects: building block of the porous framework and synthesis strategies. Graphene aerogels, CNTs aerogels, and polymer aerogels have been intensely investigated in solar vapor generation and will be discussed one by one.

Xiaozhen Hu is an assistant professor at the School of Environmental Science and Engineering, Nanjing University of Information Science and Technology, China (since September 2017). She obtained her Ph.D. degree from Zhejiang University and then worked with Prof. Jia Zhu at Nanjing University as a postdoctoral fellow. Her current research group focuses on aerogels-based energy conversion and environmental application, including solar vapor generation, water treatment, and air pollution control.

Jia Zhu is a professor at College of Engineering and Applied Science, Nanjing University, China. He received his Ph.D. degree in Electrical Engineering from Stanford University. Then he worked as a postdoctoral fellow at University of California, Berkeley and Lawrence Berkeley National Laboratory. His research interest concentrates on tailoring nanomaterials for energy and environmental applications.

2.1. Graphene-Based Aerogels

Graphene-based aerogels can be fabricated either by freeze-drying of graphene oxide (GO) based dispersion and hydrogel,[25–32] or by in situ synthesis of graphene on porous metal template.[33–35] The nanostructure of aerogels can be tuned by adjusting the synthesis parameters.

2.1.1. Freeze-Drying of GO-Based Dispersion and Hydrogel

For freeze-drying of GO-based dispersion, well-dispersed aqueous GO solution is usually used as raw materials. Water solvent is firstly frozen to ice, followed by sublimating ice to vapor, porous framework of aerogels is left. During the freeze procedure, GO sheets are concentrated at the boundary of ice

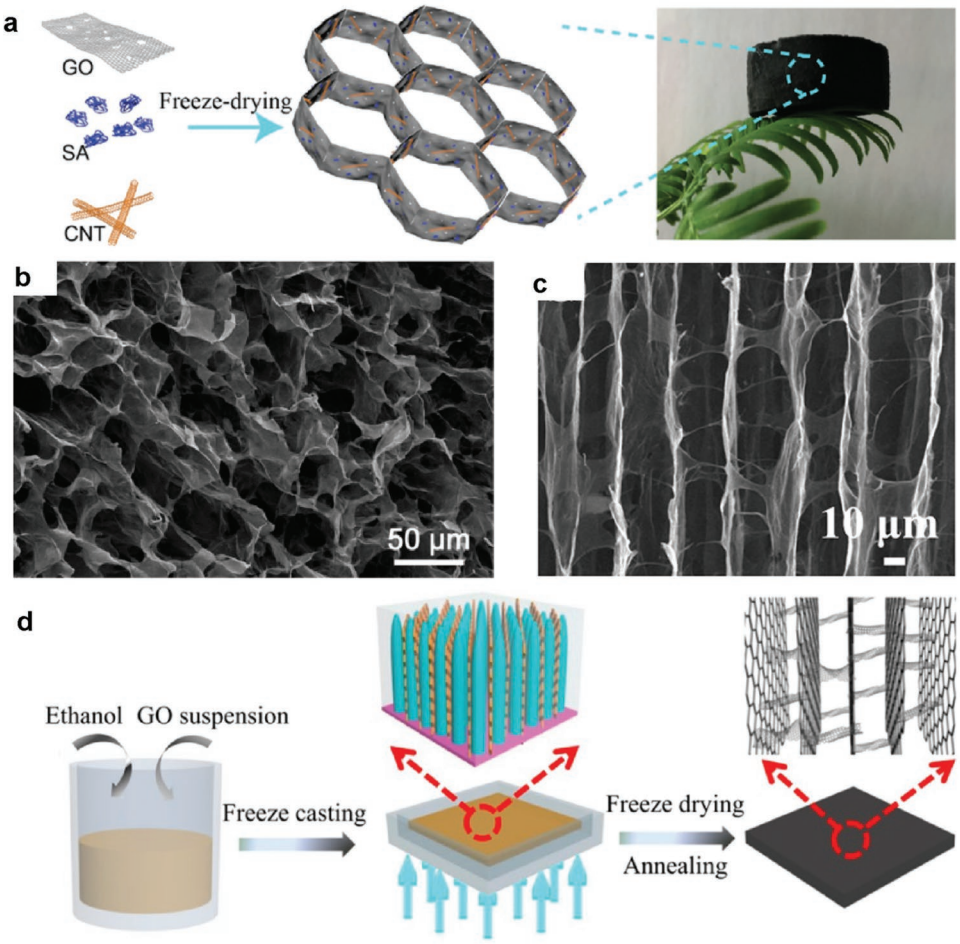

Figure 2. Synthesis procedure and microstructure of GO-based aerogels via freeze-drying strategy. a) The fabrication process of RGO-SA-CNTs aerogels. b) SEM images of RGO-SA-CNTs aerogels. c) SEM images of vertically aligned graphene aerogels. d) Schematic of the fabrication process of vertically aligned graphene aerogels. a,b) Reproduced with permission.[25] Copyright 2017, Wiley-VCH. c,d) Reproduced with permission.[26] Copyright 2017, American Chemical Society.

crystals and then align along the growth direction of ice crystals due to the squeezing effect, and honeycomb-like pore structures are obtained with the building block of GO sheets as walls after a freeze-drying procedure. Therefore, the concentration of GO solution, which is relevant with number of walls per unit, and speed of freezing process, which determines size of ice crystals, are essential for tuning pore structure of GO-based aerogels. In general, smaller pore size would be obtained by increasing GO concentration and/or accelerating the freezing procedure.

Hu et al.[25] fabricated self-floating reduced GO (RGO)-sodium alginate (SA)-CNTs composite aerogels by freeze-drying successfully (**Figure 2**a,b). Porous structure (pore size 10–30 μm, porosity 99.7%, density 0.0012–0.0176 g cm^{-3}, **Table 1**) of aerogels provided channels for water transportation, vapor escape, and ultralow thermal conductivity (<0.05 W m^{-1} K^{-1}), thus the resulting RGO-SA-CNTs aerogel enabled efficient solar vapor generation with energy conversion efficiency of 83% under 1 kW m^{-2} (water evaporation rate of 1.622 kg m^{-2} h^{-1}). Through adding ethanol into the raw aqueous GO dispersion to slow the freezing speed and tuning the growth direction of ice crystals, vertically aligned porous neat GO aerogels with many run-through channels (width of 25–35 μm, density 0.007 g cm^{-3}) were prepared (Figure 2c,d).[26] These run-through channels facilitate water transport, thus solar thermal conversion efficiency was improved to 85.6% under 1 kW m^{-2}.

By using a high precision laser, highly vertically ordered pillar array (diameter of pillar: 400 μm, spacing between pillar: 300 μm) of graphene framework with an enlarged available evaporation area and free space for fast escape of vapor was also developed (**Figure 3**a,b).[29] To construct porous graphene assemblies with un-uniform structure, 3D printing was combined with freeze-drying.[27] An all-in-one evaporator (Figure 3c, porosity 97.30%), with GO and CNTs film as light absorption layer, GO and nanofibrillated cellulose(NFC) mesh as water transporting layer, and GO/NFC wall for water uptake and thermal insulation, was printed from high concentration of GO-based ink. After being freeze-dried, self-floating porous structure was achieved, performing a high solar vapor efficiency of 85.6% under 1 kW m^{-2}.

For freeze-drying of GO-based hydrogel, GO solution is usually treated first by a hydrothermal process in a sealed container to obtain hydrogel. Followed by a freeze-drying process, porous graphene-based aerogels are achieved. During the hydrothermal process, GO sheets are normally reduced

Table 1. Pore size, porosity, density, absorption, thermal conductivity, wettability, and solar vapor generation performance of different kinds of porous materials.

Composition	Pore size [μm]	Porosity [%]	Density [g cm^{-3}]	Absorption [%]	Thermal conductivity [W m^{-1} K^{-1}]	Water contact angle [°]	Evaporation rate [kg m^{-2} h^{-1}]	Illumination density [kW m^{-2}]	Efficiency [%]
RGO-SA-CNT aerogel[25]	10–30	99.7	0.0012–0.0176	92 across 200–2500 nm	<0.05	74	1.622	1	83
Vertically aligned graphene aerogel[26]	25–35	/	0.007	93 UV, 98 Vis, Near 100 near infared	0.0038	0	1.57	1	83.56
N-doped graphene aerogel by CVD[33]	1–2	/	0.0003–0.0009	90–98 across 250–2000 nm	52 ± 6	82	1.5	1	80
All-in-one graphene evaporator by 3D printing[27]	/	97.3	/	97.2 across 250–1200 nm	0.06 (dry) 0.13 (wet)	23	1.25	1	85.6
VACNT arrays[38]	Diameter of CNTs 0.01; Neighboring CNTs 0.04–0.19	95	/	99 over 280–820 nm	/	50	≈21.5	15	90
CNT-MoS_2 film[39]	0.02–0.2	/	/	95 over 300–2500 nm	0.06	86	6.6	5	91.5
Carbonized melamine foam[45]	150	/	0.008	96.46 over 400–1200 nm	0.02856	/	1.27	1	87.3
Plasmonic wood (Pd)[57]	5–50	/	0.52	99 across 250–2500 nm	≈0.45	/	11.8	10	85
RGO-BNC/BNC bilayer aerogel[41]	/	98	0.02	96 over 400–1100 nm	0.466 (wet BNC)	/	11.8	10	83
GO film with confined 2D water path[70]	0.04	/	/	94 across 200–2500 nm	0.04 for PS-insulating foam 0.2 for GO	/	1.45	1	80
Carbonized mushrooms[56]	3.6	90	/	96 across 200–2500 nm	0.45	/	1.475	1	78

to RGO sheets, which interconnect with each other and form a cross-linked network inside, and the microstructure is formed before freeze-drying. The original concentration of GO solution, heating temperature, and heating time of the hydrothermal process are important parameters for tuning pore structure of graphene-based aerogels. Yang et al.[30] synthesized graphene aerogels by sealing ethanol solution of GO (0.5 mg mL^{-1}) in Teflon-lined autoclave at 180 °C for 12 h. Followed by solvent exchange and freeze drying, a 3D cross-linked polymer-like GO-based aerogel was achieved. The aerogel was used as standalone solar absorbers (Figure 3d, porosity >99.9%), realizing water evaporation rate of 1.3 kg m^{-2} h^{-1} under 1 kW m^{-2}.[30]

2.1.2. In Situ Growth of Graphene on Porous Metal Template

In addition to assembling GO sheets into porous framework, in situ growth of graphene platelets on porous metal template is another effective strategy to fabricate graphene aerogels. Chemical vapor deposition (CVD) is a classical method to in situ synthesized graphene on metal substrates, in which ethanol, benzene, pyridine, etc., are utilized as carbon sources. Through a high temperature process, graphene sheets are deposited on metal foils. To prepare graphene aerogels, the metal foils substrates are changed into porous metal foam templates, such as Ni foam and Cu foam. After dissolving metal foams by acid, porous graphene framework is left, thus pore structure of the obtained aerogels highly relies on the porous metal template. Ito et al.[33] synthesized 3D porous graphene by CVD with nanoporous Ni as template and benzene as carbon source. By tuning the CVD temperature from 800 to 950 °C, the averaged pore size could be tailored from 100–300 nm to 1–2 μm due to coarsening pore of Ni template at high temperature (Figure 3e,f).[33] The density of porous graphene was as low as 0.0003–0.0009 g cm^{-3}, with specific area as high as 978–1260 m^2 g^{-1}. Together with low thermal conductivity of 9–52 W m^{-1} K^{-1}, high energy conversion efficiency of 80% under 1 kW m^{-2} was achieved.

Hierarchical graphene foam was also architected by using Ni foam (pore size 400 μm) as template and methane as carbon source with plasma-enhanced CVD strategy (Figure 3g–i). The introduction of secondary structure of graphene nanoplates to the primary 3D porous structure enhanced the broadband and omnidirectional absorption of sunlight, improving energy conversion efficiency to 93.4%.[34]

Graphdiyne, with highly π-conjugated structure of sp- and sp^2-hybridized carbons, has recently appeared as a sister of graphene. Gao et al.[35] synthesized a graphdiyne-based free floating foam with graphdiyne/CuO coaxial nanowires growing on Cu foam by a solution method. The graphdiyne/CuO copper

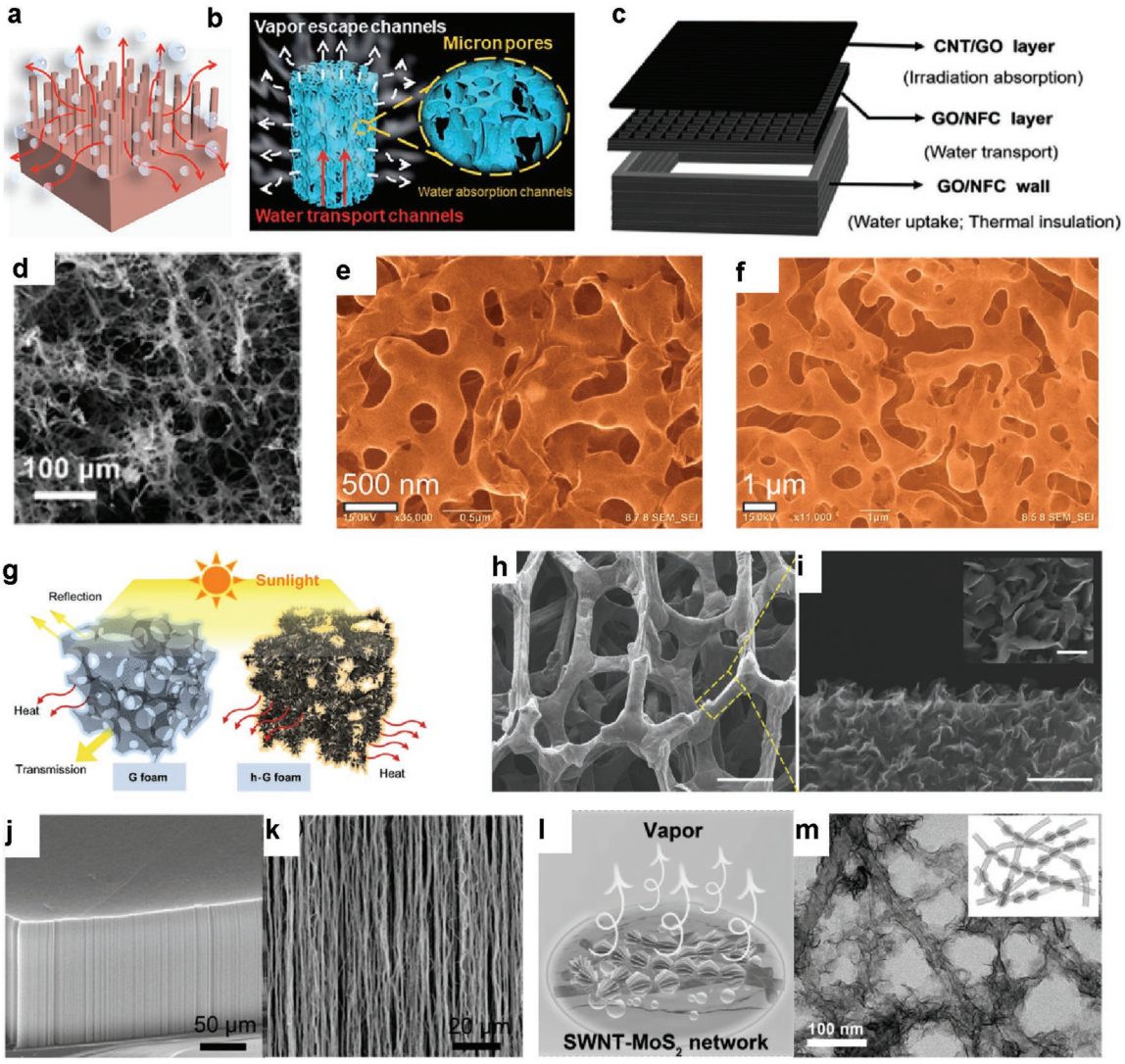

Figure 3. Structure of aerogels based on graphene and carbon nanotubes. a) Illustration of the mechanism of the solar vapor generation with the highly vertically ordered pillar array of graphene framework. b) Illustration of the mechanism of water absorption, transport, and vapor escape channels in one pillar of highly vertically ordered pillar array. c) Schematic illustration of the structure of the 3D-printed evaporator that consists of CNT/GO layer, GO/NFC layer, and GO/NFC wall. d) SEM image of the 3D graphene aerogels obtained by hydrothermal process combined with freeze-drying. e) SEM image of porous graphene with tubular structures by CVD growth at 800 °C and f) porous graphene by CVD growth at 950 °C. g) A schematic of solar-thermal conversion difference between ordinary graphene foam and hierarchical graphene foam. h) SEM image of the hierarchical graphene foam in low magnification. Scale bar: 200 μm. i) SEM image of the frame edge, inset: top view of the frame. Scale bar in (i) and (i inset): 500 and 200 nm. j) A tilted view SEM image of the VACNT array. k) A magnified side-view SEM image of the VACNT array. l) Schematic drawing of the steam generation with the SWNT-MoS_2 network. m) TEM images of the SWNT-MoS_2 network. Inset of panel (m) is the representative structural model of the SWNT-MoS_2 network. a,b) Reproduced with permission.[29] Copyright 2018, Royal Society of Chemistry. c) Reproduced with permission.[27] Copyright 2017, Wiley-VCH. d) Reproduced with permission.[30] Copyright 2018, American Chemical Society. e,f) Reproduced with permission.[33] Copyright 2015, Wiley-VCH. g–i) Reproduced with permission.[34] Copyright 2017, Wiley-VCH. j,k) Reproduced with permission.[38] Copyright 2017, American Chemical Society. l,m) Reproduced with permission.[39] Copyright 2018, Wiley-VCH.

foam was reported achieving a solar thermal conversion efficiency of 91% under 1 kW m^{-2}.[35]

2.2. CNTs-Based Aerogels

CNT is another important allotropic form of carbon nanomaterials, which is mostly synthesized by CVD. The diameter, length, and density of CNTs can be tailored by tuning the CVD parameters including size and density of catalysts, temperature, time, and so on. As a typical form of CNTs assemblies, vertically aligned CNTs (VACNTs) array, where the CNTs are aligned to form a 3D forest-like structure, exhibits absorption of about 98–99% over a large spectral range of 200 nm–200 μm,[36,37] inspiring researchers to explore the performance of CNTs array in solar energy harvesting. Yin et al.[38] synthesized extremely black VACNTs arrays (Figure 3j,k) by CVD, in which the average diameter of CNTs was about 10 nm and the interstitial spaces between neighboring CNTs were in the range of 40–190 nm (porosity 95%).[38] After generating functional groups at the end

of CNTs by plasma oxidation to improve wettability, the CNTs arrays were utilized as solar evaporator and showed high solar thermal conversion efficiency (90% under 15 kW m^{-2}).

An ultrathin (120 nm) and porous single-walled CNTs and MoS_2 sheets composite porous film (Figure 3l,m) was also synthesized by growing MoS_2 sheets on CNTs via hydrothermal reaction for interfacial solar vapor generation. MoS_2 sheets appeared flower-like nano-assemblies anchored on individual CNT, and the pore size between the CNT-MoS_2 assemblies ranged from 20 to 200 nm. The products exhibited a high evaporation efficiency (91.5% at 5 kW m^{-2}) and good cycling stability (20 times).[39]

2.3. Polymer Aerogels

Polymers can form 3D porous structures by cross-linking of polymer molecule chains. By carbonization or combination with other solar absorbers such as plasmonic particles and carbon nanomaterials to realize efficient solar absorption, polymer aerogels can be good candidates for solar vapor generation.

2.3.1. Cellulose Foams

Bacterial nanocellulose (BNC) is an attractive material ascribed to the easily formed cellulose nanofibrils (CNF). Through the classical hydrogel-based freeze-drying strategy, functional aerogels with open microporous nonwoven 3D nanofibrous structure and excellent mechanical flexibility can be architected. The diameter of CNF in BNC biofoams was in the range of 20–100 nm, and the porosity was 98% (**Figure 4**a,b). A series of photothermally active biofoams based on BNC were synthesized by incorporation of solar absorbers including plasmonic Au nanorods,[40] GO sheets,[41] and polydopamine (PDA) particles.[42] After being combined with Au nanorods to enhance solar absorption, the evaporation efficiency of 76.3% at a power density of 51 kW m^{-2} was achieved.[40]

2.3.2. Polyurethane Sponge

Polyurethane (PU) sponge, which is one kind of material with diverse industrial application due to its abundant micropores and thermal insulating property (Figure 4c),[43] is mainly prepared by polymerization of isocyanate and hydroxy compounds with the assistant of foaming agents. The ratio of foaming agent is the key factor for tailoring pore size of PU sponge. The evaporation rate of a self-floating black PU sponge with pore size of 300 μm was more than 3.5 times higher compared with that of the existing natural evaporation process. RGO sheets were introduced to PU matrix to form a cross-linked porous structure, and the as-prepared functional RGO/PU foam exhibited a photothermal efficiency of 81% at a light density of 10 kW m^{-2}.[44]

2.3.3. Melamine Foams

Melamine foams exhibit performance of high porosity, lightweight, mechanical robustness, and low thermal conductivity, making them promising candidates for efficient solar vapor generation[45,46] (Figure 4d,e). Through a high temperature calcination process, a melamine foam-based solar evaporator was obtained. The pore size could be easily tuned from 160 to 100 μm by increasing the calcination temperature from 400 to 700 °C, and the highest energy conversion efficiency of 87.3% under 1 kW m^{-2} was realized with pore diameter of 150 μm and porosity of 99%.

Papavassiliou and coworkers[47] also produced melamine-based carbon sponges through a scalable and low-cost in-air calcination process, which achieved a high energy conversion efficiency of 92% under 1 kW m^{-2}. In addition, the obtained sponges exhibited promising anti-fouling capability, which remained stable during 30 h under 1 kW m^{-2} with artificial wastewater composed of soil, salt, and acid.

2.3.4. Polyacrylamide-Based Aerogels

Hydrophilic polyacrylamide-based aerogels with hierarchical structure of radially aligned channels, micron pores, wrinkled internal surface, and molecular meshes were fabricated via radial ice-templated assembly and UV-initiated cryopolymerization.[48] The tree-inspired design benefited aerogels excellent capillary rise function, realizing a quick (1.08 cm at 1 s) and long-distance (>28 cm) water transportation. After being combined with CNTs, the bilayer aerogel achieved energy conversion efficiency of 85.7% under 1 kW m^{-2}.

2.3.5. Other Polymer Foams

Other polymers can also be solution processed into self-floating monolithic foams, which can be used as solar evaporators.[49,50] A typical example is manufacturing charged porous polymer membranes by using anion in poly (ionic liquid) (Figure 4f). Heteroatom-doped hierarchically porous polymer membrane could be fabricated, and the pore size was found well controlled from >20 to 0.6 μm by rational choice of anions in poly (ionic liquid). After carbonization, the porous carbon membrane (pore diameter ≈7, 0.75 μm; specific area, 158–499 m^2 g^{-1}) was obtained and used as solar absorber for seawater desalination.[50]

Aerogels and related 3D architectures based on graphene, CNTs, and polymers can be synthesized by different strategies and pore structure can be tailored by tuning synthesis parameters to enable efficient solar evaporation. In addition to tailoring pore structure, the performance of interfacial solar vapor generation can be optimized by optical management, thermal management, and wettability enhancement. In the following sections, we will summarize the efforts on tailoring aerogels and related 3D macroporous monoliths for solar vapor generation from these three main points.

3. Optical Management

Excellent absorption across solar spectrum (300–2500 nm) is a prerequisite for efficient solar vapor generation. For aerogels, the absorption can be calculated by using the following equation:

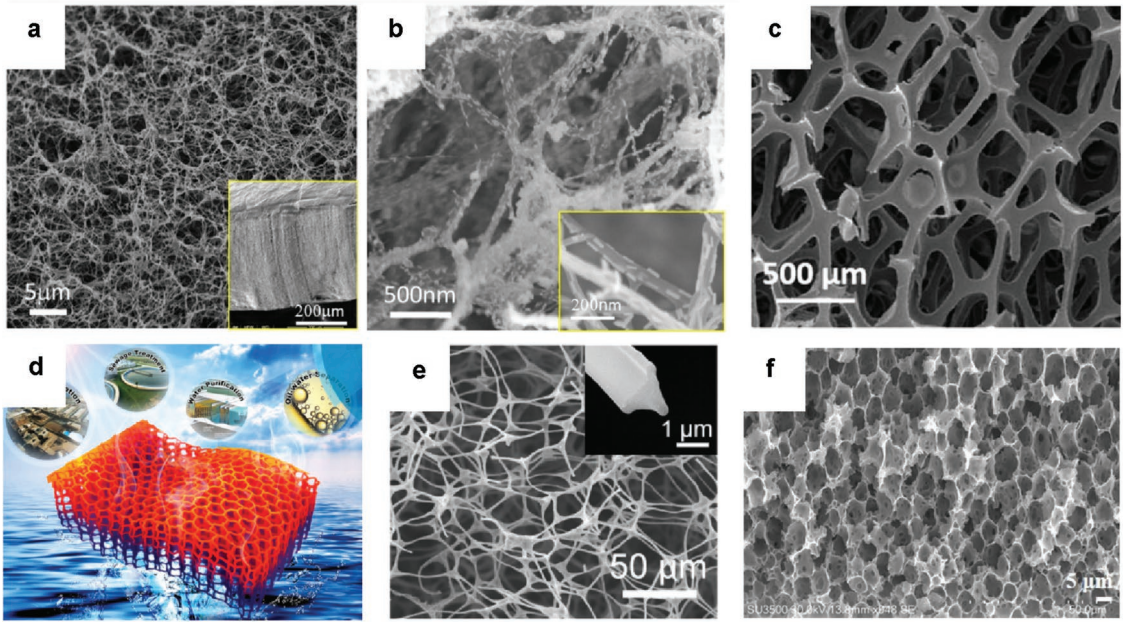

Figure 4. Structure of polymer-based aerogels. a) Cross-section of plasmonic aerogel depicting the preserved highly open porous structure, which ensures the accessibility of the plasmonic nanostructures and b) corresponding high-resolution image of plasmonic aerogel cross-section revealing dense and uniform adsorption of AuNRs on the nanofibers of the BNC aerogel (inset shows individual fibers decorated with AuNRs). c) SEM image of pristine black PU sponge. d) Schematic of melamine foams. e) SEM images of carbonized sponge, inset: corresponding cross-sectional image of carbon sponge fibrils. f) Cross-sectional SEM image of charged porous polymer membrane. a,b) Reproduced with permission.[40] Copyright 2016, American Chemical Society. c) Reproduced with permission.[43] Copyright 2017, Elsevier. d) Reproduced with permission.[45] Copyright 2018, Royal Society of Chemistry. e) Reproduced with permission.[46] Copyright 2018, Wiley-VCH. f) Reproduced with permission.[50] Copyright 2018, American Chemical Society.

$$\alpha = 1 - R - T \tag{3}$$

where α represents absorption, R is the reflection, and T is the transmission. Both R and T can be measured by using an integrating sphere. According to Equation (3), an ideal absorber for solar evaporation should eliminate R and T. As described by Fresnel's law, incident light from air (refractive index $n_0 = 1.0003$) onto a surface of refractive index, n, reflects with the reflectance:

$$R = (n - n_0)^2 / (n + n_0)^2 \tag{4}$$

The equation implies that the reflection is suppressed when the refractive index of a sample is close to that of air. For most of dense solid materials, the refractive indexes are larger than 1.3. Aiming to reduce the refractive index, porous solid material in which air replaces part of solid is a good choice originating from the decreased electron density and permissivity.[37] As one kind of representative porous solids, aerogels possess >85% volume of air, which naturally exhibit suppressed reflection.

The porous structure can also increase the light propagation distance inside samples through multiple scattering. Compared with relatively smooth surface of solids, aerogels normally exhibit rough surface, which randomizes the light propagation direction inside the material. The effect of total internal reflection results in a much longer optical path length inside materials and hence a substantial absorption enhancement.[36] If the particle size and/or pore diameter is comparable or even smaller than wavelength scale, the absorption enhancement factor can even go far beyond the theoretical limit.[51] Therefore, aerogels reveal enhanced absorption ascribed to the suppressed reflection and increased light propagation distance, which is favorable for solar harvesting applications.

Recent report on optical management of aerogels for solar vapor generation mainly concentrates on carbon-based materials and plasmonic absorbers. Carbon-based materials including carbon nanomaterials and carbonized materials usually exhibit blackbody-like absorption across the full solar spectrum, which are very suitable for solar vapor generation. For plasmonic absorbers, broadband and efficient absorption can be realized by high density of hybridized localized surface plasmon resonance and efficient reflection reduction through tuning size and/or shape of plasmonic nanoparticles.[18,21]

3.1. Carbon Nanomaterials

Carbon nanomaterials for solar vapor generation mainly consist of CNTs, graphene, carbon black nanoparticles,[52] and so on. 3D honeycomb-like RGO-SA-CNT aerogel exhibited an averaged ≈92% absorption across 200–2500 nm,[25] benefiting from both the intrinsic absorption of RGO, CNT, and its honeycomb porous structure with reduced reflection and enhanced optical path length (**Figure 5**a). Attributing to the unique structure of abundant voids and imperfect alignment, VACNTs showed extremely black characteristics with 99% absorbance across 280–820 nm.[38] The coarse surface trapped the solar light into the array, which was continuously deflected among the CNTs.

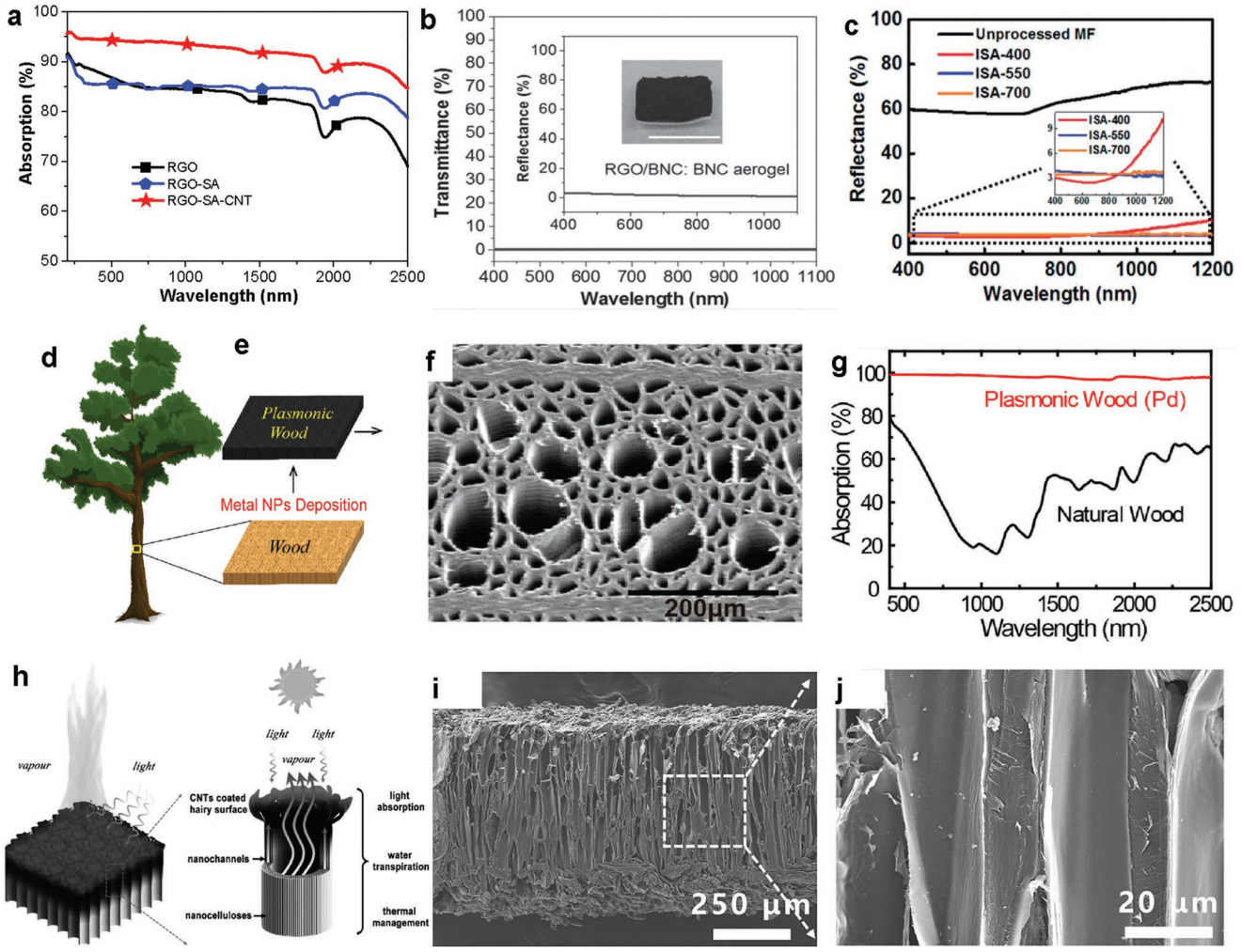

Figure 5. Optical management of aerogels. a) Solar absorption spectrum of RGO, RGO-SA, and RGO-SA-CNT aerogels. b) Transmittance and reflectance spectra of RGO/BNC:BNC aerogel. Inset: photographs of the RGO/BNC:BNC aerogel. The scale bar represents 1 cm. c) The reflectance spectra of unprocessed melamine foam (MF), integrative solar absorbers (ISA)-400, ISA-550, and ISA-700. Inset image: the partial reflectance spectra of ISA-400, ISA-550, and ISA-700. d) A tree transports water from the bottom upward and absorbs sunlight for photosynthesis. e) After nanoparticle decoration, the natural wood is cut perpendicular to the growth direction of the tree and turns black due to the plasmonic effect of the metal nanoparticles. f) SEM image of top view of plasmonic wood. The diameter of microchannels varies from 5 to 50 μm. g) Representative absorption curves for plasmonic wood decorated with Pd nanoparticles and natural wood. h) Graphical illustration of the flexible solar vapor made from carbon nanotubes-coated flexible wood membrane. i,j) Cross-section-view images that show the multichannels. a) Reproduced with permission.[25] Copyright 2017, Wiley-VCH. b) Reproduced with permission.[41] Copyright 2016, Wiley-VCH. c) Reproduced with permission.[45] Copyright 2018, Royal Society of Chemistry. d–g) Reproduced with permission.[57] Copyright 2018, Wiley-VCH. h–j) Reproduced with permission.[58] Copyright 2017, Wiley-VCH.

Combined with other aerogels, bilayered structures with porous CNTs or GO assemblies as absorbing layer for solar vapor generation were reported. Wang's group designed a bilayered structure with macroporous silica substrate at the bottom layer for water transportation and heat insulation, and the top porous CNTs layer for solar absorption.[53] With optimized thickness of the CNTs top layer, nearly full light harvesting with average diffuse reflection less than 2% and almost zero transmission was achieved. Another bilayer all-nanofiber aerogel with CNTs as absorbing layer was also employed for efficient vapor generation. The upper CNTs layer showed good solar absorption performance (97.5% across 300–1200 nm), and the bottom layer that consisted of naturally abundant NFC could realize sustainability and biodegradability.[54] The bilayer aerogel showed a solar-energy conversion efficiency of 76.3% and water evaporation rate of 1.11 kg m^{-2} h^{-1} at 1 kW m^{-2}. GO was also introduced to the cellulose fibrous structure, and the bilayered hybrid biofoam composed of BNC and RGO for solar vapor generation exhibited large optical extinction (96%, Figure 5b).[41] The evaporation efficiency of the RGO/BNC:BNC aerogel was calculated to be 83% at a power density of 10 kW m^{-2}.

3.2. Carbonized Materials

Through high-temperature carbonization of polymer foams, graphitic carbon can be obtained, which can effectively enhance the optical absorption.[46] A typical example is melamine foam.

The original melamine foam had a reflectance up to 63.9%, while after calcination under 400, 550, 700 °C, the reflectance dramatically decreased to 3.52–4.23%. The transmittance was less than 0.02%, indicating strong light absorption of carbonized melamine foams (95.75–96.46%, Figure 5c).[45] Through a simple dip-coating process, GO sheets were coated on melamine skeletons. N-doped graphene and carbon hybrid aerogels were synthesized after a carbonization treatment (600 °C), performing a higher averaged absorption of 97.57% across 200–2500 nm.[55] In addition, the absorption of several natural materials can also be improved through carbonization. A natural mushroom had an absorption of 79% across 200–2500 nm, which could be dramatically increased to 96% through carbonization due to the reduced reflection.[56]

3.3. Plasmonic Nanoparticles

Apart from carbon-based materials, plasmonic nanoparticles are another kind of representative solar absorbers for vapor generation. By tuning the size of plasmonic nanoparticles, high absorption (99% absorption across 250–2500 nm) could be realized by assembling Pd nanoparticles into porous wood (pore size, 5–50 μm).[57] The excellent solar absorption performance was mainly attributed to high density of hybridized localized surface plasmon resonance of Pd nanoparticles with random size and efficient reflection reduction. Following the same guideline, Au and Ag plasmonic nanoparticles were also combined with porous wood, and high absorption of solar energy was achieved.

3.4. Other Absorbers

PDA, formed by oxidation of dopamine, possesses many striking properties of naturally occurring eumelanin due to the structural similarity. For example, it can absorb 99% incident photon energy over a broad solar spectrum and rapidly convert it into heat within tens of picoseconds.[42] Combined with BNC aerogel, a bilayer evaporator with a large optical extinction (98%) was fabricated.

Wood shows mesoporous, low tortuosity, and hierarchical structure, which makes it suitable for solar vapor generation.[57–61] Various absorbers including plasmonic nanoparticles, CNTs, GO, graphite, and PDA were combined with natural wood to improve the light-harvesting property (Figure 5d–j),[57,58] showing good absorption (>95%).[57,58,60] Other porous structures including cotton,[62,63] ceramic fiber wool,[64] Al foam,[65] were also utilized as framework, and solar absorbers were fabricated after carbonization[63] or addition of CuS nanocages,[62] TiN nanoparticles,[64] and exfoliated graphite.[60,65]

In addition, MXene, a new series of 2D materials composed of early transition metal carbides and/or carbonitrides, were found exhibiting ultrahigh internal light-to-heat conversion efficiency, which was measured to be 100% for Ti_3C_2.[66] A thin MXene membrane successfully produced a light-to-water evaporation efficiency of 84% under 1 kW m^{-2}. Through hierarchical structure design of MXene by mimicking the black scales of Bitis rhinoceros, both enhanced light-to-heat conversion for solar steam generation (86.7% under 1 kW m^{-2}) and wearable thermal devices could be realized.[67] Metal sulfide including MoS_2,[68] CuS,[62] and Cu_7S_4[69] was also utilized for solar vapor generation, achieving portable or mercury-removal devices.[68]

4. Thermal Management

According to Equation (2), efficient solar vapor generation of aerogels not only requests efficient absorption of solar energy, but also needs suppressed heat losses including conduction, convection, and radiation. In this section, we will analyze the thermal performance of aerogels, and summarize the recent progress on reducing heat losses from two aspects of decreasing thermal conductivity and multiple devices through materials design and device design.

4.1. Thermal Conductivity of Aerogels

Heat transport in aerogels is caused mainly by three parts: 1) thermal conduction, consisting of solid skeleton conduction and gas conduction, 2) convection, and 3) infrared radiation. **Figure 6**a shows the contributions to thermal conductivity of a GO-based foam with oriented pores.[24] The total thermal conductivity λ_T can be approximated by the sum of solid, gas, convection, and irradiation conductivity:

$$\lambda_T = \lambda_s + \lambda_g + \lambda_c + \lambda_r \tag{5}$$

The solid conduction of the cell wall can be estimated by a weighted average of the effective solid conduction values of the individual components of the nanocomposite foam by using:

$$\lambda_s = \frac{\lambda^*}{\lambda^* \frac{R_K}{d} + 1} \tag{6}$$

The gaseous conductivity λ_g can be estimated according to:

$$\lambda_g = \frac{\lambda_{g0}\Pi}{2\beta K_n + 1} \quad K_n = \frac{l_g}{\delta} \tag{7}$$

where λ_{g0} is the gas conductivity of free space, Π is the porosity, β is relevant with the energy transfer between gas molecules and the limiting structure (for air in aerogels, $\beta \approx 2$), K_n is the Knudsen number, which equals to the ratio of mean free path of a gas molecule l_g and the pore diameter δ.

Taking a typical GO-CNF-sepiolite nanorods composite foam as an example,[24] the gaseous conductivity was calculated to be approximately below 0.001 W m^{-1} K^{-1}, and the solid conductivity was below 0.04 W m^{-1} K^{-1} in the radical direction (for comparison, the thermal conductivity of air is 0.024 W m^{-1} K^{-1} at 298 K). It was also proved that the experimental thermal conductivity λ_T of aerogels was mainly composed of solid conduction (λ_s) and gas conduction (λ_g), as is shown in Figure 6b, and the total thermal conductivity of aerogels was highly relevant with density.[4] The ultralow thermal conductivity of

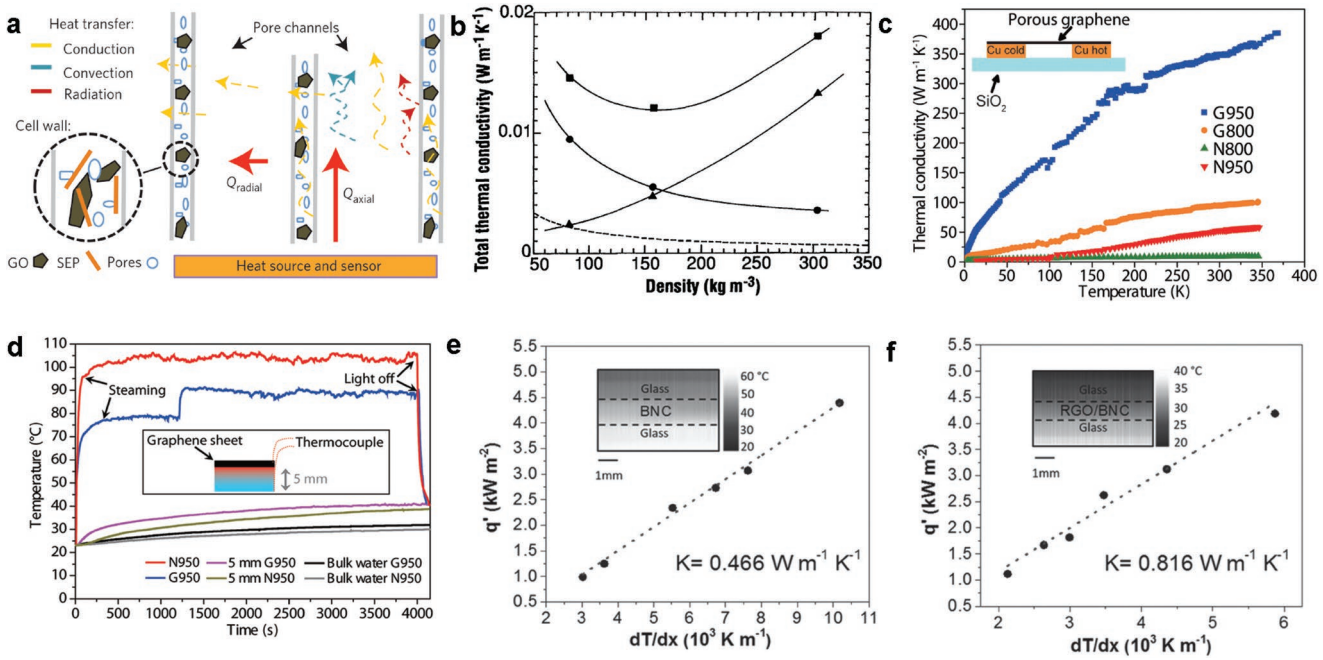

Figure 6. Thermal performance of several typical aerogels. a) Schematic illustration of contributions to thermal conductivity in the radial and axial directions of GO-based foam with oriented pores. b) Total conductivity (■), calculated radiative conductivity (---), gaseous conductivity (●), and solid conductivity (▲), of resorcinol-formaldehyde aerogels as a function of density at ambient conditions. c) Thermal conductivity of porous graphene samples in the temperature range of 2–370 K. The graphene samples were overpassed on two Cu wires with four prove terminals on a SiO_2 substrate. Both horizontal and vertical error bars are within their symbols. d) The temperature rise of porous graphene samples under 9 kW m^{-2} solar illumination. The steam was obviously generated from the surface within 2 min. The solar illumination shut down after 4000 s. e) Thermal conductivity of wet BNC aerogel and f) wet RGO/BNC aerogel. Insets: representative IR images showing the temperature gradient along the thickness of the hydrated BNC and RGO/BNC layers. a) Reproduced with permission.[24] Copyright 2015, Springer Nature. b) Reproduced with permission.[4] Copyright 1992, American Association for the Advancement of Science. c,d) Reproduced with permission.[33] Copyright 2015, Wiley-VCH. e,f) Reproduced with permission.[41] Copyright 2016, Wiley-VCH.

aerogels can effectively localize heat in small vapor generation area, without heating the whole sample or the underlying bulk water.

4.2. Materials Design

According to Equations (6) and (7), the thermal conductivity of aerogels can be reduced by decreasing the particle size (d) and the pore diameter (δ), and/or increasing the interfacial thermal resistance of nanosized components (R_K). GO-based aerogels exhibit low thermal conductivity attributing to the highly porous structure. For example, RGO-SA-CNT aerogels with RGO sheets of 0.5–5 µm (pore size: 10–30 µm) showed thermal conductivity of <0.05 W m^{-1} K^{-1} at 298 K,[25] which was only slightly higher than that of air (0.024 W m^{-1} K^{-1}). Decreasing size of the graphene sheets can reduce the thermal conductivity of graphene aerogels. Following this principle, small-size, defect-abundant graphene (0.2–3 µm) based aerogels were synthesized by laser reduction, and the thermal conductivity was found as low as 0.0075 W m^{-1} K^{-1}.[28] Compared with graphene aerogels synthesized from GO by solution strategy, graphene foams obtained by CVD method usually show higher thermal conductivity (9–349 W m^{-1} K^{-1}) (Figure 6c),[33] mainly ascribed to the large size, almost defect-free structure of graphene sheets, and intense stacking between the neighboring sheets (decreased R_K). By tuning pore size from 1–2 µm to 259 nm, the thermal conductivity of porous graphene obtained by CVD can be reduced from 52 to 9 W m^{-1} K^{-1} successfully.[33]

Attributing to the low thermal conductivity of aerogels, heat generated from solar irradiation could be effectively localized in a small region near the sample, without heating the water below. Take N-doped porous graphene as an example, the temperature of sample quickly reached 100 °C within 300 s, whereas the temperature of water below the sample only slightly increased to about 40 °C after 1 h illumination at 9 kW m^{-2} (Figure 6d).

To further enhance heat localization, a typical double layer structure was designed with two different layers as solar-absorbing layer and thermal-insulating layer.[17] For example, Jiang et al.[41] fabricated a bilayered biofoam with RGO/BNC composite layer as solar-absorbing layer and BNC aerogel layer as thermal-insulating layer. The thermal conductivity of wetted BNC aerogel was calculated to be 0.466 W m^{-1} K^{-1} (Figure 6e), which is lower than that of wet RGO/BNC composite aerogel layer (0.816 W m^{-1} K^{-1}, Figure 6f). The good thermal-insulating property of the bottom BNC aerogel layer could effectively prevent generated heat in upper solar-absorbing RGO/BNC composite layer from dissipating into the bulk water by conduction. Thus solar energy was successfully localized in the evaporation region, yielding a solar thermal conversion efficiency of 83% at 10 kW m^{-2} solar illumination. To follow up

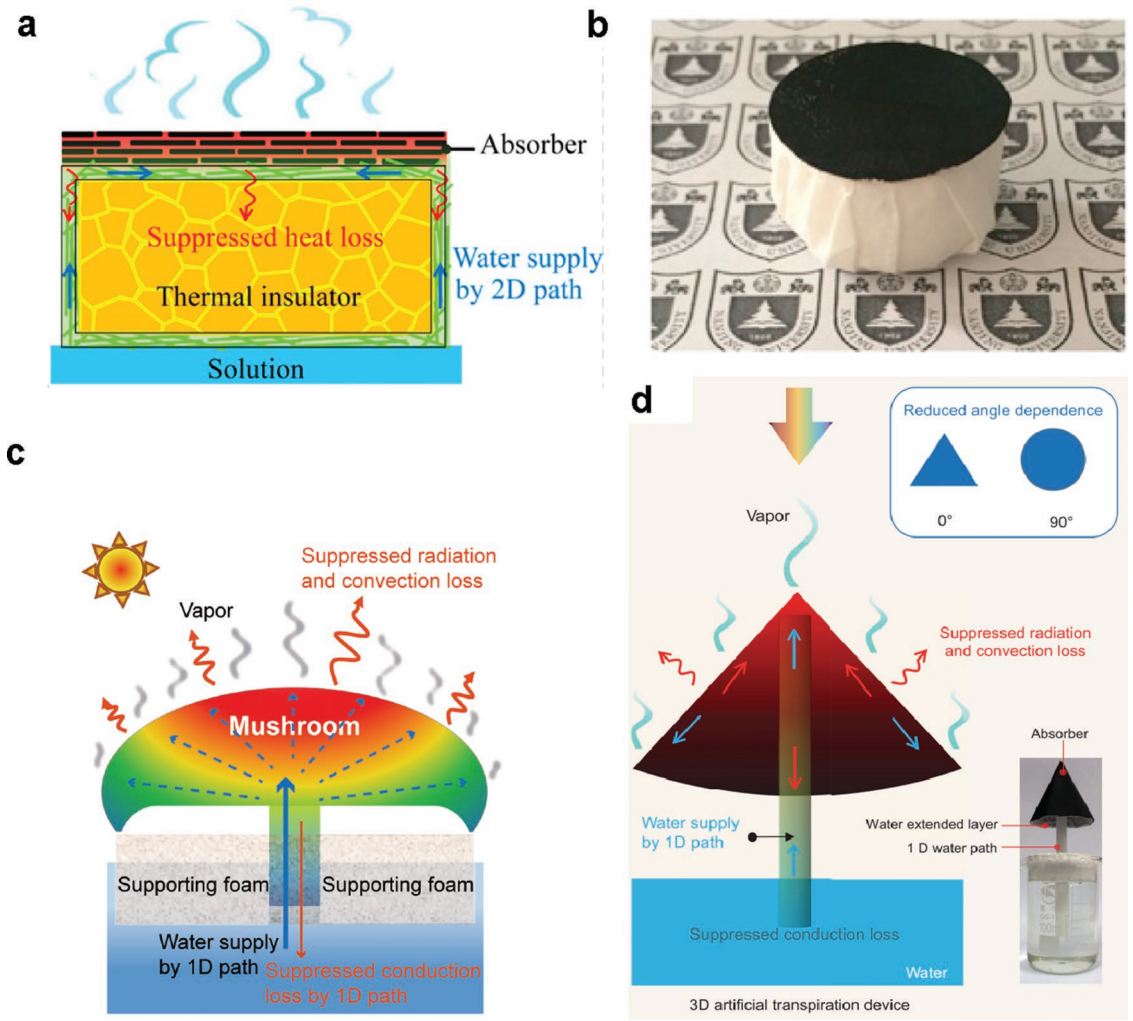

Figure 7. Thermal management by device design. a) Schematics of solar evaporation devices with suppressed heat loss and 2D water supply. b) The physical map of polystyrene foam (thermal insulator), cellulose (2D water path) wrapped over the surface of polystyrene foam, and GO film (absorber) on the top surface. c) Schematic of the heat behavior in a mushroom-based structure. d) Schematics of the 3D artificial transpiration device with suppressed heat loss. a,b) Reproduced with permission.[70] Copyright 2016, National Academy of Sciences. c) Reproduced with permission.[56] Copyright 2018, Wiley-VCH. d) Reproduced with permission.[71] Copyright 2018, Oxford Academic.

this design, many other bilayered aerogels with CNTs[53,54,58] and RGO[61] as absorbing layer, and CNF aerogels,[54] porous wood,[58,61] and silica aerogels[53] as thermal-insulating layer were prepared for heat localization of solar vapor generation systems.

4.3. Device Design

Apart from reducing thermal conductivity of aerogels absorbers to realize heat localization, combing the heat insulating-porous foams with confined water path to form integrated device is another effective way to minimize heat losses of solar evaporation system. Various porous substances including hydrophobic-expanded polyethylene (EPE) and polystyrene (PS) foams have been utilized as the insulation layer to reduce heat losses. Combined with 2D- or 1D-confined water path design, the device can reach higher solar-to-vapor efficiency due to the suppressed heat losses of water transporter to the underlying water through conduction and convection.

Zhu's group demonstrated a smart design with PS foam as thermal insulator, and cellulose coating as confined 2D water path (**Figure 7**a,b).[70] Attributing to the reduced dimensionality of water path, the heat dissipation through water transporter was decreased, and the device showed efficient (80% under 1 kW m^{-2}) and effective (four orders salinity decrement) solar desalination performance.

Natural mushrooms were found to be an ideal solar vapor generation device.[56] The umbrella-shaped black pileus with a large surface-projected area ratio enabled stronger evaporation and consequently smaller temperature increase, resulting in suppressed convection (4%) and radiation (4%) losses. The fibrous stipe confined the water path in a quasi-1D with a small cross-section, leading to a minimized conduction loss of less than 1% (Figure 7c). Through a carbonization process, mushrooms reached 78% conversion efficiency under 1 kW m^{-2}

attributing to the unique natural 3D structure and suppressed three components of heat losses. Inspired by the perfect mushrooms model for solar vapor generation, Li et al.[71] further developed a 3D artificial transpiration device with 1D water supply, minimized heat loss by PS foam, and 3D design of absorber (Figure 7d), achieving 85% solar vapor efficiency under 1 kW m^{-2}.

Other designs of the device with PS foam as insulation layer have been also reported, including multilevel device to obtain higher water productivity,[72] foam-air combined insulation layer,[73] and so on.[74] EPE foam was also utilized in solar vapor generation device for heat insulation, achieving a high conversion efficiency of 91.3% under 1 kW m^{-2}.[75]

5. Wettability Enhancement

In addition to efficient solar absorption and suppressed heat losses, effective water transportation is also critical for interfacial solar vapor generation. There are mainly two steps for water transportation of aerogels: wetted by water and pumping water from below to the evaporation region by capillary force. Wettability is evaluated by water contact angle, which is highly relevant with the composition and micro/nano-structure of the surface. If the water contact angle of aerogels is smaller than 90°, the aerogels can be partially or fully wetted by water. As tailoring pore structure has been summarized in the Section 2, we will introduce several methods to improve the wettability of aerogels by tuning the composition, mainly including O plasma introducing hydrophilic oxygen-contained groups, utilizing hydrophilic additives, and so on.

5.1. O plasma

Fu et al.[32] utilized oxygen plasma to introduce oxygen implant into hydrophobic graphene aerogels with a water contact angle of 137°, and the treated graphene aerogels demonstrated fine hydrophilicity, which could be wetted within 50 ms (**Figure 8**a–f).[32] Superhydrophobic VACNTs array (water contact angle 153°) was also successfully transformed into hydrophilic by plasma treatment, with a contact angle of around 50° (Figure 8g–i).[38]

5.2. Hydrophilic Additives

Besides oxygen plasma, the wettability of carbon based aerogels can also be improved by nitrogen doping. Ito et al.[33] synthesized N-doped graphene with pyridine as nitrogen source by CVD, and at the same synthesis conditions, N-doped graphene aerogels showed much better hydrophilic performance (water contact angle 82°) compared with the neat graphene aerogels (115°).[33] Hydrophilic polymers can also act as additives to enhance the wettability of aerogels. A hydrophilic natural biopolymer, SA, was added into the RGO aerogels, and the water contact angle decreased from 115° to 74°, indicating the improved hydrophilicity.[25]

5.3. Other Methods

Monolithic carbon-aerogel networks consisting of randomly aggregated hollow-carbon-nanotubes (HCNTs) with 100–250 nm in diameter and a length of up to several micrometers were synthesized by facile carbonization of conjugated micro-porous polymer nanotubes.[76] The hierarchically nanoporous network exhibited broad light absorption (99%), low thermal conductivity (0.192 W m^{-1} K^{-1}), and abundant porosity (92%) with open channel structure, which was very suitable for solar vapor generation. However, it was hard for the as-prepared carbon aerogels to be fully wetted by water due to the intrinsic carbon skeleton. After being treated by ammonium peroxydisulfate-saturated 1 M H_2SO_4, the oxygen atomic concentration increased from 3.42% to 11.63%, and the water droplet could be fully impregnated within 6 s. Thus a high conversion efficiency of 86.8% was achieved under 1 kW m^{-2}.

6. Summary and Outlook

Aerogels and related 3D macroporous architectures have been intensely pursued as one kind of the most promising absorbers for efficient interfacial solar vapor generation, attributing to the intrinsic highly porous structure, lightweight, enhanced absorption, and low thermal conductivity. In the past few years, various aerogels including GO, CNTs, polymers, and so on have been introduced to this field to achieve good solar evaporation performance. Compared with the original, noble, metal-based solar absorbers, carbon-based absorbers consisting of graphene, CNTs-based aerogels, polymer foams, and carbonized materials exhibit advantages of relatively low cost, broadband solar absorption, chemical stability, and environmental friendliness.[77] Ultra-lightweight graphene-based aerogels with tunable nanostructure and extremely low thermal conductivity can be scalable synthesized through facile freeze-drying of GO dispersion, though the price of GO powder from Sigma-Aldrich is 122 \$ g^{-1}, which is calculated to be 1220 \$ m^{-2} for graphene aerogel with typical height of 2 mm, density of 0.005 g cm^{-3}. Benefit from the extremely black performance, CNTs assemblies for solar vapor generation have attracted much attention. However, CNTs are usually obtained by CVD, highly increasing the cost of CNTs-based absorbers (\$521 for one CNTs array on Si substrate from Sigma-Aldrich). Polymer foams (e.g., 12.5 \$ m^{-2} for calcinated melamine sponge)[47] are much more cost-effective and flexible than nanocarbon-based aerogels, yet only several typical polymers including cellulose, melamine, and PU can be utilized to synthesize foams. Carbonized materials, especially for biochar (e.g., ≈5 \$ kg^{-1} for mushrooms), are introduced to solar vapor generation systems mainly attributing to the excellent biocompatibility and hierarchical micro-nano porous structure and/or smart natural design, while the density is much larger than aerogels, and the flexibility as well as scalability needs to be further improved.

In this review, we summarized the efforts on tailoring aerogels and related 3D macroporous monoliths for efficient solar evaporation through structural designs, optical management, thermal management, and wettability enhancement. The design principles of structure and composition in improving

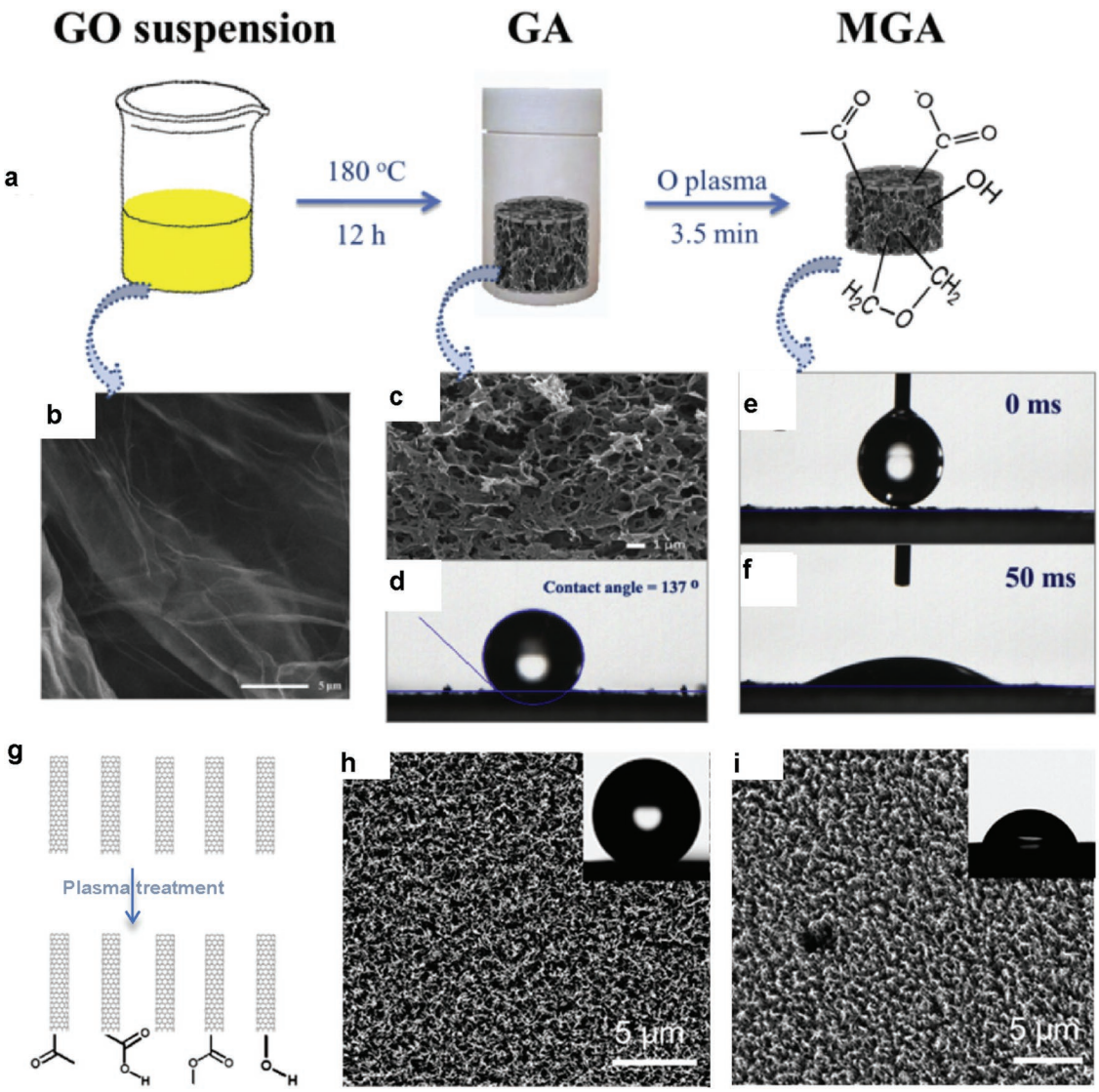

Figure 8. Wettability enhancement of aerogels. a) Schematic illustration showing the fabrication of the hydrophilic-modified graphene aerogel. SEM images of b) GO and c) graphene aerogel. Water contact angles of d) the graphene aerogel and e,f) the modified graphene aerogel during different shooting times. g) Schematic illustration showing the plasma treatment of VACNT arrays. h) Top-view SEM images of an as-grown VACNT array and i) a treated VACNT array. The insets show the contact angle of water on the surface. a–f) Reproduced with permission.[32] Copyright 2018, Elsevier. g–i) Reproduced with permission.[38] Copyright 2017, American Chemical Society.

optical absorption, wettability, and decreasing thermal conductivity have been discussed and typical examples were provided. Despite the great achievements, there are still challenges which need more efforts in future studies.

1) To meet the challenge of water scarcity, high water evaporation rate is preferred. As the conversion efficiency of solar to vapor is approaching the theoretical limit in recent publications, it is necessary to find ways to further increase the evaporation rate. One efficient way is exploiting environmental energy to enhance the performance well above the theoretical limit (100%) through careful structural design. As a typical example, Li et al.[78] demonstrated a hierarchical evaporator with arrays of cotton cores wrapped with hydrophilic cellulose, which was coated with carbon black nanoparticles for absorption, and successfully improved water evaporation rate to 2.4, 1.5, 1.1 times of theoretical values for light intensities of 0.25, 0.5, 1 kW m^{-2}, respectively.

Another possible way to increase the evaporation rate is to reduce water vaporization enthalpy according to Equation (1). Following this principle, Yu and co-workers[79] found that the solar energy conversion of hierarchically nanostructured polymer hydrogel was induced by the light-absorbing polymer penetrating the molecular meshes of the gel, which provided an efficient in situ energy utilization system with significantly reduced vaporization enthalpy (**Figure 9**). Thus a high evaporation rate of 3.2 kg m^{-2} h^{-1} via 94% solar energy of 1 kW m^{-2} was realized. Hydratable PVA and chitosan networks[80] as well as PVA-Ti_2O_3

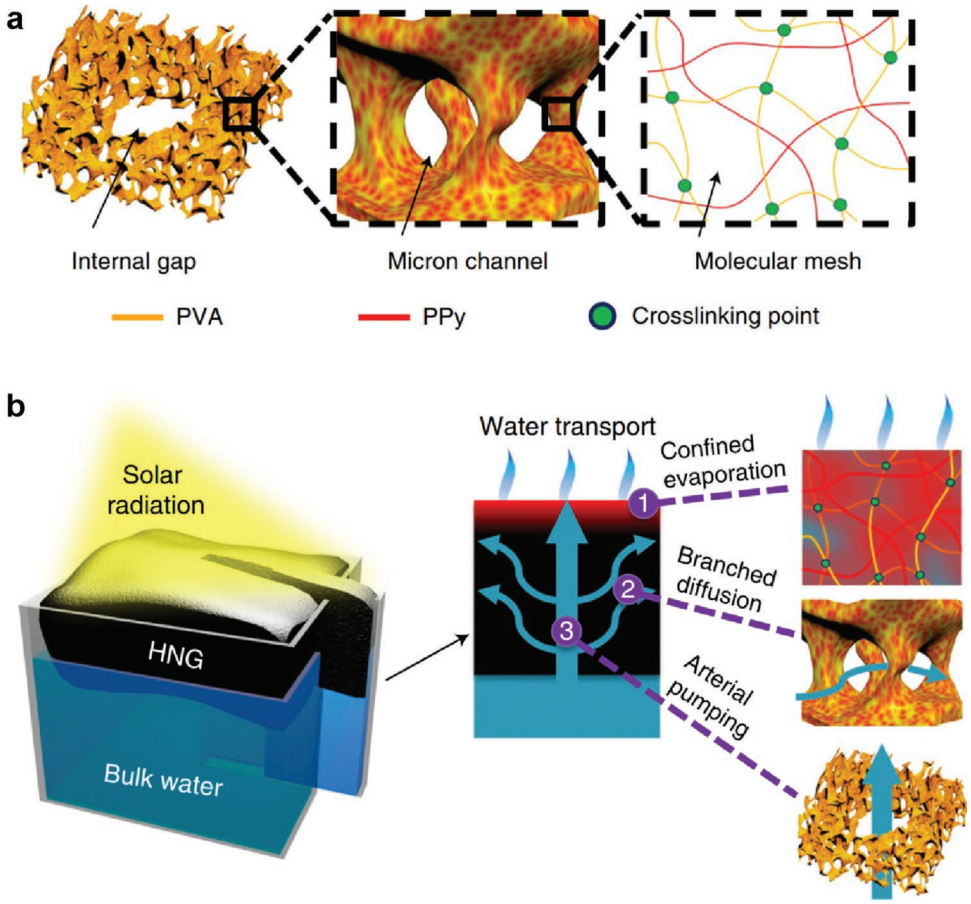

Figure 9. Schematic of highly efficient solar vapor generation based on tailored water transport in hierarchical nanostructured gel (HNG). a) The HNG consists of hierarchical porous structures, including internal gaps, micron channels, and molecular meshes, wherein the solar absorber (PPy) penetrates the polyvinyl alcohol (PVA) network of the gel. b) Schematic of a typical solar vapor generation system and the water confinement strategy. Under solar radiation, the solar absorbers in the molecular meshes of the floating generator are heated, facilitating the evaporation of water confined in the polymeric network (1). The water confined in the molecular mesh has a reduced evaporation enthalpy. The evaporated water can be rapidly recovered via branched water diffusion (2) and pumping (3) based on micron channels and internal gaps, respectively. a,b) Reproduced with permission.[79] Copyright 2018, Springer Nature.

nanoparticles hydrogel[81] were subsequently synthesized, and it was found that these structures could further improve water evaporation rate to 3.6 $kg\,m^{-2}\,h^{-1}$ under 1 kW m^{-2}. In addition, plasmonic Ag nanoparticles-based double-layer hydrogel (agarose) device was also fabricated to enhance water evaporation rate.[82]

2) Apart from high evaporation rate, the long term stability of aerogels structure as well as performance is essential during practical applications such as wastewater treatment and solar desalination. However, recent researches revealed that it was seemingly unavoidable of fouling or salt accumulation on the absorbers, which would destroy the porous structure of aerogels and seriously accelerate the degradation of performance. Smart designs of mechanically strong aerogels with salt rejection and/or anti-fouling property are urgently needed. Recent studies in bio-inspired structural design of water lily[83] demonstrate initial progress in stable evaporation of high salinity brine. Wood with hierarchical porous structure[84] also exhibits salt-resistant property, and self-regenerating evaporator can be fabricated by designing a rational artificial channel array in a natural wood substrate.[85] For anti-fouling applications, inorganic nanomaterials such as MXene nanosheets[86] and copper-zinc-tin-selenide nanocarambolas[87] were utilized as solar absorbers.
3) Benefit from the advantages of high energy conversion efficiency, clean and sustainable solar energy input, as well as zero contaminants output, interfacial solar vapor generation technology has been widely applied in the fields of solar desalination,[52] wastewater treatment,[71] electricity generation,[88–90] sterilization,[91] and so on (**Figure 10**). However, these researches are still in early stage, and the performance needs to be constantly improved, especially for aerogels absorber. Also more attention should be paid to minimize the gap between the lab-scale systems and practical applications in daily life. For example, when applied on the surface of large area water such as in ocean or lake, it is still a challenge for absorbers to spread/assemble easily. Possible routes involve combining commercial flexible substrates such as 3D cotton towel[92] and cellulose paper[93,94] with organic solar-absorbing materials, and robust,

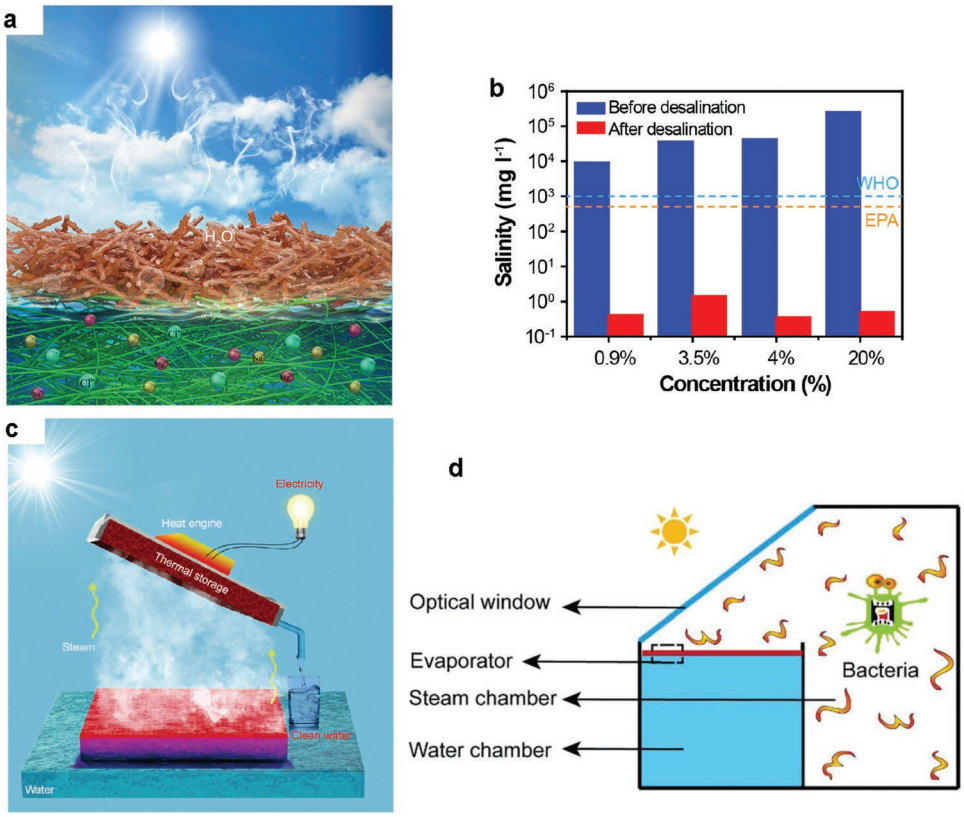

Figure 10. Applications of interfacial solar vapor generation. a) Schematic of mechanism of solar desalination based on Janus absorber. b) The measured salinities (the weight percentage of Na^+) of the four simulated seawater samples before and after desalination. c) Storage and recycling of interfacial solar vapor enthalpy for simultaneous generation of clean water and electricity. d) Schematic of the interfacial-heating-based solar autoclave for bacterial sterilization. a,b) Reproduced with permission.[52] Copyright 2018, Wiley-VCH. c) Reproduced with permission.[90] Copyright 2018, Elsevier. d) Reproduced with permission.[91] Copyright 2018, Wiley-VCH.

foldable, and large area absorbers can be achieved. Besides, special attention needs to be paid to the scalability and cost of solar vapor generation systems for practical applications.[95–97]

In addition, it is very necessary to expand more applications of interfacial solar evaporation and integrate with mature technologies such as solar photovoltaic,[98] photocatalysis,[99] thermal electric,[100,101] batteries, and so on. It is expected that, through extensive efforts, aerogels-based interfacial solar vapor generation can not only provide solution of world-wide clean water scarcity problem, but also play a dominant role in effective usage of the abundant solar energy in near future.

Acknowledgements

This work was funded by the State Key Program for Basic Research of China (No. 2015CB659300), National Natural Science Foundation of China (No. 11874211, 11574143, 21805132, 11621091, 61735008), Natural Science Foundation of Jiangsu Province (No. BK20160630, BK20180341), the Fundamental Research Funds for the Central Universities (No. 021314380135, 021314380128), and the Startup Foundation of Nanjing University of Information Science and Technology (No. 2243141701084, 2017r084).

Conflict of Interest

The authors declare no conflict of interest.

Keywords

aerogels, interfacial solar vapor generation, optical and thermal management, pore structures, wettability

Received: September 2, 2019
Revised: October 3, 2019
Published online:

[1] S. Kistler, *Nature* **1931**, *127*, 741.
[2] C. Morris, M. Anderson, R. Stroud, C. Merzbacher, D. Rolison, *Science* **1999**, *284*, 622.
[3] J. Ryan, A. Berry, M. Anderson, J. Long, R. Stroud, V. Cepak, V. Browning, D. Rolison, C. Merzbacher, *Nature* **2000**, *406*, 169.
[4] X. Lu, M. Arduini-Schuster, J. Kuhn, O. Nilsson, J. Fricke, R. Pekala, *Science* **1992**, *255*, 971.
[5] T. Schaedler, A. Jacobsen, A. Torrents, A. Sorensen, J. Lian, J. Greer, L. Valdevit, W. Carter, *Science* **2011**, *334*, 962.

[6] A. Cao, P. Dickrell, W. Sawyer, M. Ghasemi-Nejhad, P. Ajayan, *Science* **2005**, *310*, 1307.
[7] Z. Chen, W. Ren, L. Gao, B. Liu, S. Pei, H. Cheng, *Nat. Mater.* **2011**, *10*, 424.
[8] H. Sun, Z. Xu, C. Gao, *Adv. Mater.* **2013**, *25*, 2554.
[9] H. D. Gesser, P. C. Goswami, *Chem. Rev.* **1989**, *89*, 765.
[10] N. Hüsing, U. Schubert, *Angew. Chem. Int. Ed.* **1998**, *37*, 22.
[11] N. Hüsing, U. Schubert, *Ullmann's Encyclopedia of Industrial Chemistry*, Wiley-VCH, Weinheim, Germany **2012**.
[12] J. Fricke, A. Emmerling, *Adv. Mater.* **1991**, *3*, 10.
[13] J. Biener, M. Stadermann, M. Suss, M. Worsley, M. Biener, K. Rose, T. Baumann, *Energy Environ. Sci.* **2011**, *4*, 656.
[14] Y. Qin, Q. Peng, Y. Ding, Z. Lin, C. Wang, Y. Li, F. Xu, J. Li, Y. Yuan, X. He, Y. Li, *ACS Nano* **2015**, *9*, 8933.
[15] B. Wang, W. Abdulla, D. Wang, X. Zhao, *Energy Environ. Sci.* **2015**, *8*, 869.
[16] S. Cui, W. Cheng, X. Shen, M. Fan, A. Russell, Z. Wu, X. Yi, *Energy Environ. Sci.* **2011**, *4*, 2070.
[17] H. Ghasemi, G. Ni, A. Marconnet, J. Loomis, S. Yerci, N. Miljkovic, G. Chen, *Nat. Commun.* **2014**, *5*, 4449.
[18] L. Zhou, Y. Tan, J. Wang, W. Xu, Y. Yuan, W. Cai, S. Zhu, J. Zhu, *Nat. Photon.* **2016**, *10*, 393.
[19] Y. Liu, S. Yu, R. Feng, A. Bernard, Y. Liu, Y. Zhang, H. Duan, W. Shang, P. Tao, C. Song, T. Deng, *Adv. Mater.* **2015**, *27*, 2768.
[20] L. Zhang, B. Tang, J. Wu, R. Li, P. Wang, *Adv. Mater.* **2015**, *27*, 4889.
[21] L. Zhou, X. Li, G. Ni, S. Zhu, J. Zhu, *Natl. Sci. Rev.* **2019**, *6*, 562.
[22] G. Ni, G. Li, S. Boriskina, H. Li, W. Yang, T. Zhang, G. Chen, *Nat. Energy.* **2016**, *1*, 16126.
[23] S. Kistler, A. Caldwell, *Ind. Eng. Chem.* **1934**, *26*, 6.
[24] B. Wicklein, A. Kocjan, G. Salazar-Alvarez, F. Carosio, G. Camino, M. Antonietti, L. Bergström, *Nat. Nanotechnol.* **2015**, *10*, 277.
[25] X. Hu, W. Xu, L. Zhou, Y. Tan, Y. Wang, S. Zhu, J. Zhu, *Adv. Mater.* **2017**, *29*, 1604031.
[26] P. Zhang, J. Li, L. Lv, Y. Zhao, L. Qu, *ACS Nano* **2017**, *11*, 5087.
[27] Y. Li, T. Gao, Z. Yang, C. Chen, W. Luo, J. Song, E. Hitz, C. Jia, Y. Zhou, B. Liu, B. Yang, L. Hu, *Adv. Mater.* **2017**, *29*, 1700981.
[28] P. Zhang, Q. Liao, T. Zhang, H. Cheng, Y. Huang, C. Yang, C. Li, L. Jiang, L. Qu, *Nano Energy* **2018**, *46*, 415.
[29] P. Zhang, Q. Liao, H. Yao, H. Cheng, Y. Huang, C. Yang, L. Jiang, L. Qu, *J. Mater. Chem. A* **2018**, *6*, 15303.
[30] Y. Yang, R. Zhao, T. Zhang, K. Zhao, P. Xiao, Y. Ma, P. Ajayan, G. Shi, Y. Chen, *ACS Nano* **2018**, *12*, 829.
[31] Y. Fu, G. Wang, T. Mei, J. Li, J. Wang, X. Wang, *ACS Sustainable Chem. Eng.* **2017**, *5*, 4665.
[32] Y. Fu, G. Wang, X. Ming, X. Liu, B. Hou, T. Mei, J. Li, J. Wang, X. Wang, *Carbon* **2018**, *130*, 250.
[33] Y. Ito, Y. Tanabe, J. Han, T. Fujita, K. Tanigaki, M. Chen, *Adv. Mater.* **2015**, *27*, 4302.
[34] H. Ren, M. Tang, B. Guan, K. Wang, J. Yang, F. Wang, M. Wang, J. Shan, Z. Chen, D. Wei, H. Peng, Z. Liu, *Adv. Mater.* **2017**, *29*, 1702590.
[35] X. Gao, H. Ren, J. Zhou, R. Du, C. Yin, R. Liu, H. Peng, L. Tong, Z. Liu, J. Zhang, *Chem. Mater.* **2017**, *29*, 5777.
[36] Z. Yang, L. Ci, J. A. Bur, S. Lin, P. M. Ajayan, *Nano Lett.* **2008**, *8*, 446.
[37] K. Mizuno, J. Ishii, H. Kishida, Y. Hayamizu, S. Yasuda, D. N. Futaba, M. Yumura, K. Hata, *Proc. Natl. Acad. Sci. USA* **2009**, *106*, 6044.
[38] Z. Yin, H. Wang, M. Jian, Y. Li, K. Xia, M. Zhang, C. Wang, Q. Wang, M. Ma, Q. Zheng, Y. Zhang, *ACS Appl. Mater. Interfaces* **2017**, *9*, 28596.
[39] X. Yang, Y. Yang, L. Fu, M. Zou, Z. Li, A. Cao, Q. Yuan, *Adv. Funct. Mater.* **2018**, *28*, 1704505.
[40] L. Tian, J. Luan, K. Liu, Q. Jiang, S. Tadepalli, M. Gupta, R. Naik, S. Singamaneni, *Nano Lett.* **2016**, *16*, 609.
[41] Q. Jiang, L. Tian, K. Liu, S. Tadepalli, R. Raliya, P. Biswas, R. Naik, S. Singamaneni, *Adv. Mater.* **2016**, *28*, 9400.
[42] Q. Jiang, H. Derami, D. Ghim, S. Cao, Y. Jun, S. Singamaneni, *J. Mater. Chem. A* **2017**, *5*, 18397.
[43] S. Ma, C. Chiu, Y. Zhu, C. Tang, H. Long, W. Qarony, X. Zhao, X. Zhang, W. Lo, Y. Tsang, *Appl. Energy* **2017**, *206*, 63.
[44] G. Wang, Y. Fu, A. Guo, T. Mei, J. Wang, J. Li, X. Wang, *Chem. Mater.* **2017**, *29*, 5629.
[45] X. Lin, J. Chen, Z. Yuan, M. Yang, G. Chen, D. Yu, M. Zhang, W. Hong, X. Chen, *J. Mater. Chem. A* **2018**, *6*, 4642.
[46] L. Zhu, M. Gao, C. Peh, X. Wang, G. Ho, *Adv. Energy Mater.* **2018**, *8*, 1702149.
[47] F. Gong, H. Li, W. Wang, J. Huang, D. Xia, J. Liao, M. Wu, D. Papavassiliou, *Nano Energy* **2019**, *58*, 322.
[48] W. Xu, Y. Xing, J. Liu, H. Wu, Y. Cui, D. Li, D. Guo, C. Li, A. Liu, H. Bai, *ACS Nano* **2019**, *13*, 7930.
[49] Q. Chen, Z. Pei, Y. Xu, Z. Li, Y. Yang, Y. Wei, Y. Ji, *Chem. Sci.* **2018**, *9*, 623.
[50] Y. Shao, Z. Jiang, Y. Zhang, T. Wang, P. Zhao, Z. Zhang, J. Yuan, H. Wang, *ACS Nano* **2018**, *12*, 11704.
[51] Z. Yu, A. Raman, S. Fan, *Proc. Natl. Acad. Sci. USA* **2010**, *107*, 17491.
[52] W. Xu, X. Hu, S. Zhuang, Y. Wang, X. Li, L. Zhou, S. Zhu, J. Zhu, *Adv. Energy Mater.* **2018**, *8*, 1702884.
[53] Y. Wang, L. Zhang, P. Wang, *ACS Sustainable Chem. Eng.* **2016**, *4*, 1223.
[54] F. Jiang, H. Liu, Y. Li, Y. Kuang, X. Xu, C. Chen, H. Huang, C. Jia, X. Zhao, E. Hitz, Y. Zhou, R. Yang, L. Cui, L. Hu, *ACS Appl. Mater. Interfaces* **2018**, *10*, 1104.
[55] B. Huo, D. Jiang, X. Cao, H. Liang, Z. Liu, C. Li, J. Liu, *Carbon* **2019**, *142*, 13.
[56] N. Xu, X. Hu, W. Xu, X. Li, L. Zhou, S. Zhu, J. Zhu, *Adv. Mater.* **2017**, *29*, 1606762.
[57] M. Zhu, Y. Li, F. Chen, X. Zhu, J. Dai, Y. Li, Z. Yang, X. Yan, J. Song, Y. Wang, E. Hitz, W. Luo, M. Lu, B. Yang, L. Hu, *Adv. Energy Mater.* **2018**, *8*, 1701028.
[58] C. Chen, Y. Li, J. Song, Z. Yang, Y. Kuang, E. Hitz, C. Jia, A. Gong, F. Jiang, J. Zhu, B. Yang, J. Xie, L. Hu, *Adv. Mater.* **2017**, *29*, 1701756.
[59] X. Wu, G. Chen, W. Zhang, X. Liu, H. Xu, *Adv. Sustainable Syst.* **2017**, *1*, 1700046.
[60] T. Li, H. Liu, X. Zhao, G. Chen, J. Dai, G. Pastel, C. Jia, C. Chen, E. Hitz, D. Siddhartha, R. Yang, L. Hu, *Adv. Funct. Mater.* **2018**, *28*, 1707134.
[61] K. Liu, Q. Jiang, S. Tadepalli, R. Raliya, P. Biswas, R. Naik, S. Singamaneni, *ACS Appl. Mater. Interfaces* **2017**, *9*, 7675.
[62] X. Wu, M. Robson, J. Phelps, J. Tan, B. Shao, G. Owens, H. Xu, *Nano Energy* **2019**, *56*, 708.
[63] X. Wu, L. Wu, J. Tan, G. Chen, G. Owens, H. Xu, *J. Mater. Chem. A* **2018**, *6*, 12267.
[64] M. Kaur, S. Ishii, S. Shinde, T. Nagao, *ACS Sustainable Chem. Eng.* **2017**, *5*, 8523.
[65] S. Sajadi, N. Farokhnia, P. Irajizad, M. Hasnain, H. Ghasemi, *J. Mater. Chem. A* **2016**, *4*, 4700.
[66] R. Li, L. Zhang, L. Shi, P. Wang, *ACS Nano* **2017**, *11*, 3752.
[67] K. Li, T. Chang, Z. Li, H. Yang, F. Fu, T. Li, J. Ho, P. Chen, *Adv. Energy Mater.* **2019**, *9*, 1901687.
[68] W. Li, M. Tekell, Y. Huang, K. Bertelsmann, M. Lau, D. Fan, *Adv. Energy Mater.* **2018**, *32*, 1802108.
[69] X. Li, Z. Yao, J. Wang, D. Li, K. Yu, Z. Jiang, *ACS Appl. Energy Mater.* **2019**, *2*, 5154.
[70] X. Li, W. Xu, M. Tang, L. Zhou, B. Zhu, S. Zhu, J. Zhu, *Proc. Natl. Acad. Sci. USA* **2016**, *113*, 13953.
[71] X. Li, R. Lin, G. Ni, N. Xu, X. Hu, B. Zhu, G. Lv, J. Li, S. Zhu, J. Zhu, *Nat. Sci. Rev.* **2018**, *5*, 70.

[72] G. Xue, Q. Chen, S. Lin, J. Duan, P. Yang, K. Liu, J. Li, J. Zhou, *Glob. Chall.* **2018**, *2*, 1800001.
[73] H. Song, Y. Liu, Z. Liu, M. Singer, C. Li, A. Cheney, D. Ji, L. Zhou, N. Zhang, X. Zeng, Z. Bei, Z. Yu, S. Jiang, Q. Gan, *Adv. Sci.* **2018**, *5*, 1800222.
[74] L. Shi, Y. Wang, L. Zhang, P. Wang, *J. Mater. Chem. A* **2017**, *5*, 16212.
[75] P. Liu, L. Miao, Z. Deng, J. Zhou, H. Su, L. Sun, S. Tanemura, W. Cao, F. Jiang, L. Zhao, *Mater. Today Energy* **2018**, *8*, 166.
[76] P. Mu, Z. Zhang, W. Bai, J. He, H. Sun, Z. Zhu, W. Liang, A. Li, *Adv. Energy Mater.* **2019**, *9*, 1802158.
[77] S. Cao, Q. Jiang, X. Wu, D. Ghim, H. Derami, P. Chou, Y. Jun, S. Singamaneni, *J. Mater. Chem. A* **2019**, *7*, 24092.
[78] X. Li, J. Li, J. Lu, N. Xu, C. Chen, X. Min, B. Zhu, H. Li, L. Zhou, S. Zhu, T. Zhang, J. Zhu, *Joule* **2018**, *2*, 1331.
[79] F. Zhao, X. Zhou, Y. Shi, X. Qian, M. Alexander, X. Zhao, S. Mendez, R. Yang, L. Qu, G. Yu, *Nat. Nanotech.* **2018**, *13*, 489.
[80] X. Zhou, F. Zhao, Y. Guo, B. Rosenberger, G. Yu, *Sci. Adv.* **2019**, *5*, 5484.
[81] Y. Guo, X. Zhou, F. Zhao, J. Bae, B. Rosenberger, G. Yu, *ACS Nano* **2019**, *13*, 7913.
[82] Z. Sun, J. Wang, Q. Wu, Z. Wang, Z. Wang, J. Sun, C. Liu, *Adv. Funct. Mater.* **2019**, *29*, 1901312.
[83] N. Xu, J. Li, Y. Wang, C. Fang, X. Li, Y. Wang, L. Zhou, B. Zhu, Z. Wu, S. Zhu, J. Zhu, *Sci. Adv.* **2019**, *5*, 7013.
[84] S. He, C. Chen, Y. Kuang, R. Mi, Y. Liu, Y. Pei, W. Kong, W. Gan, H. Xie, E. Hitz, C. Jia, X. Chen, A. Gong, J. Liao, J. Li, Z. Ren, B. Yang, S. Das, L. Hu, *Energy Environ. Sci.* **2019**, *12*, 1558.
[85] Y. Kuang, C. Chen, S. He, E. Hitz, Y. Wang, W. Gan, R. Mi, L. Hu, *Adv. Mater.* **2019**, *31*1900498.
[86] X. Zha, X. Zhao, J. Pu, L. Tang, K. Ke, R. Bao, L. Bai, Z. Liu, M. Yang, W. Yang, *ACS Appl. Mater. Interfaces* **2019**, *11*, 40.
[87] Y. Yang, W. Que, J. Zhao, Y. Han, M. Ju, X. Yin, *Chem. Eng. J.* **2019**, *373*, 955.
[88] L. Cui, P. Zhang, Y. Xiao, Y. Liang, H. Liang, Z. Cheng, L. Qu, *Adv. Mater.* **2018**, *30*, 1706805.
[89] P. Yang, K. Liu, Q. Chen, J. Li, J. Duan, G. Xue, Z. Xu, W. Xie, J. Zhou, *Energy Environ. Sci.* **2017**, *10*, 1923.
[90] X. Li, X. Min, J. Li, N. Xu, P. Zhu, B. Zhu, S. Zhu, J. Zhu, *Joule* **2018**, *2*, 1.
[91] J. Li, M. Du, G. Lv, L. Zhou, X. Li, L. Bertoluzzi, C. Liu, S. Zhu, J. Zhu, *Adv. Mater.* **2018**, *30*, 1805159.
[92] Y. Yang, Y. Sui, Z. Cai, B. Xu, *Glob. Chall.* **2019**, *3*, 1900004.
[93] F. Ni, P. Xiao, C. Zhang, Y. Liang, J. Gu, L. Zhang, T. Chen, *ACS Appl. Mater. Interfaces* **2019**, *11*, 15498.
[94] W. Li, Z. Li, K. Bertelsmann, D. Fan, *Adv. Mater.* **2019**, *31*, 1900720.
[95] H. Wilson, ShakeelurR. , A. Parab, N. Jha, *Desalination* **2019**, *456*, 85.
[96] Y. Chen, Y. Shi, H. Kou, D. Liu, Y. Huang, Z. Chen, B. Zhang, *ACS Sustainable Chem. Eng.* **2019**, *7*, 2911.
[97] C. Li, D. Jiang, B. Huo, M. Ding, C. Huang, D. Jia, H. Li, C. Liu, J. Liu, *Nano Energy* **2019**, *60*, 841.
[98] W. Wang, Y. Shi, C. Zhang, S. Hong, L. Shi, J. Chang, R. Li, Y. Jin, C. Ong, S. Zhuo, P. Wang, *Nat. Commun.* **2019**, *10*, 3012.
[99] S. Lu, F. Liu, P. Qiu, M. Qiao, Y. Li, Z. Cheng, N. Xue, X. Hou, C. Xu, Y. Xiang, F. Peng, Z. Guo, *Chem. Eng. J.* **2020**, *379*, 122382.
[100] L. Zhu, T. Ding, M. Gao, C. Peh, G. Ho, *Adv. Energy Mater.* **2019**, *9*, 1900250.
[101] Y. Zhang, S. Ravi, S. Tan, *Nano Energy* **2019**, *65*, 104006.